2D Materials

PAPER

Observation of two-dimensional superconductivity in an ultrathin iron–arsenic superconductor

RECEIVED
1 December 2020

REVISED
1 January 2021

ACCEPTED FOR PUBLICATION
8 January 2021

PUBLISHED
28 January 2021

Chi Zhang[1,2,3], Tao Hu[4], Teng Wang[1,2,5], Yufeng Wu[4], Aobo Yu[1,2,3], Jianan Chu[1,2,3], Han Zhang[1,2,3], Xuefu Zhang[1], Hong Xiao[6], Wei Peng[1,2,3], Zengfeng Di[1,3], Shan Qiao[1,2,3] and Gang Mu[1,2,3]

[1] State Key Laboratory of Functional Materials for Informatics, Shanghai Institute of Microsystem and Information Technology, Chinese Academy of Sciences, Shanghai 200050, People's Republic of China
[2] CAS Center for Excellence in Superconducting Electronics (CENSE), Shanghai 200050, People's Republic of China
[3] University of Chinese Academy of Sciences, Beijing 100049, People's Republic of China
[4] Beijing Academy of Quantum Information Sciences, Beijing 100193, People's Republic of China
[5] School of Physical Science and Technology, ShanghaiTech University, Shanghai 201210, People's Republic of China
[6] Center for High Pressure Science and Technology Advanced Research, Beijing 100094, People's Republic of China

E-mail: hutao@baqis.ac.cn **and** mugang@mail.sim.ac.cn

Keywords: ultrathin, iron–arsenic superconductor, two-dimensional superconductivity, $KCa_2Fe_4As_4F_2$

Supplementary material for this article is available online

Abstract

Two-dimensional (2D) superconductors supply important platforms for exploring new quantum physics and high-T_c superconductivity. The intrinsic superconducting properties in the 2D iron–arsenic superconductors are still unknown owing to the difficulties in the preparation of ultrathin samples. Here we report the fabrication and physical investigations of the high quality single-crystalline ultrathin films of the iron–arsenic superconductor $KCa_2Fe_4As_4F_2$. For the sample with the thickness of 2.6–5 nm (1–2 unit cells), a sharp superconducting transition at around 30 K (onset point) is observed. Compare with the bulk material, the ultrathin sample reveals a relatively lower T_c, wider transition width, higher anisotropy, broader flux liquid region under the in-plane field, and smaller thermal activated energy with a 2D feature. Moreover, the angle dependent upper critical field follows the Tinkham model, demonstrating the two-dimensional superconductivity in ultrathin $KCa_2Fe_4As_4F_2$. The significant dimensionality effect observed here is markedly different from those observed in cuprate superconductors.

1. Introduction

Two-dimensional superconductivity draw great interests due to the emergence of new quantum phenomena [1–3], including Ising superconductivity [4–6], quantum metallic state [7–10], Berezinskii–Kosterlitz–Thouless (BKT) transition [11, 12], and even the significant enhancement of T_c [13–15]. From the material point of view, most of the 2D superconductors (2DSCs) under investigation belong to the transition metal disulfide compounds [4–6, 14, 15], which have the easy-to-exfoliated layered structure. Owing the unconventional superconducting (SC) properties and the high T_c, the 2D behaviors of cuprates [16] and iron-based superconductors [17] are worth studying. For the cuprates, mechanical exfoliation method was adopted to create the ultrathin $Bi_2Sr_2CaCu_2O_{8+x}$ (Bi2212) superconductor in recent years [18–22]. A rather high-T_c very close to the bulk compound [19–22] and the absence of dimensionality effect [21] were revealed in this system. As for the iron-based superconductors, investigations focus on the iron–selenic (FeSe, including $FeSe_{1-x}Te_x$) materials by the method of the precisely controlled molecular beam-epitaxy (MBE) growth [13] or mechanical exfoliation [23, 24]. During this process, high temperature superconductivity was observed in the single-layer FeSe film grown on $SrTiO_3$ substrates [13]. On the other hand, the iron–arsenic (FeAs) system has a more diverse crystal structure and higher T_c [17, 25–28]. Thus, revealing the performance in terms of dimensionality effect and T_c variation in 2D limit is very crucial in understanding the intrinsic properties of this system.

However, due to the stronger inter-layer coupling, as compared with the Bi2212 and iron–selenic systems, it has been a huge challenge for a long time

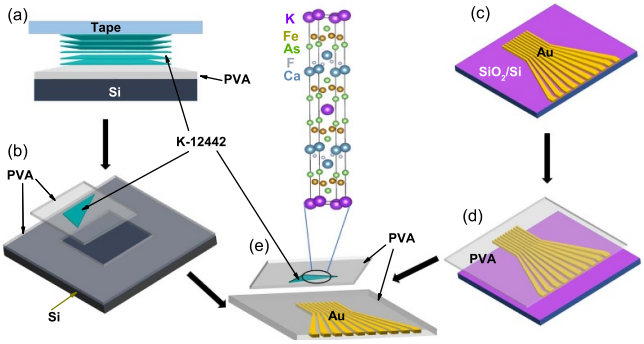

Figure 1. The fabrication process for device of ultrathin K-12442. (a) PVA-assisted mechanical exfoliation of K-12442 sample. (b) Transferring the PVA film and ultrathin K-12442 sample from the substrate. (c) Prefabricated Au electrodes on Si/SiO_2 substrate by ultraviolet lithography and metal thermal evaporation. (d) Peeling off the Au electrodes using PVA. (e) The upper and lower layers of PVA film encapsulate the sample and Au electrodes to obtain device of ultrathin K-12442.

to obtain the ultrathin samples in the iron–arsenic system. The recently reported 12442 system [28–32], which has double FeAs layers between neighboring insulating layers, reveals a very large resistivity anisotropy ratio ($\rho_c/\rho_{ab} \approx 3150$) [33]. This value is much larger than those of other iron–arsenic superconductors [34, 35], indicating a rather weak inter-layer coupling. Using an improved mechanical exfoliation method, we successfully fabricated the ultrathin films of $KCa_2Fe_4As_4F_2$ (K-12442) with the thickness down to 1–2 unit cells. Here we report the mechanical exfoliation and superconducting properties of the ultrathin K-12442, which are compared with the bulk samples. By examining the angle dependence of the upper critical field, a clear two-dimensional feature is revealed in the ultrathin samples, which is in sharp contrast with the bulk samples. The present work provides an important platform to study the dimensionality effect of unconventional superconductors, which is rather different with the cuprate system.

2. Experimental section

The K-12442 single crystals were grown by the self-flux method [36]. We adopted an improved mechanical exfoliation method to fabricate the ultrathin samples of K-12442. The traditional process of mechanical exfoliation uses the silicon-based (SiO_2/Si) substrate [19, 21], which has insufficient adhesion to some materials with a strong inter-layer coupling. Thus it is difficult to obtain ultra-thin samples by this traditional method in many quasi-2D materials. Here we use an organic substrates, polyvinyl alcohol (PVA), to replace silicon-based substrates to enhance the adhesion without changing the characteristics of the materials. PVA has a relatively stronger adhesion and is typically used to transfer 2D materials [37]. The advantage of strong adhesion for this material is utilized in the process of mechanical exfoliation in this work.

Figure 1 shows the fabricating process for ultrathin K-12442 sample devices. First, the self-made PVA solution with the concentration of 8% is dripped on a silicon substrate to cover the entire substrate surface, which stands for 5 h in a drying oven to evaporate the water in the PVA solution naturally. In this way we obtained a smooth PVA film with a certain thickness and adhesion on the silicon substrate. Next, a fresh surface of layered K-12442 crystal was cleaved from blue tape, which was put onto the PVA substrate. Afterwards, a more adhesive tape was used to thin the K-12442 flakes on the PVA substrate for 2–3 times until we obtained the ultrathin K-12442 sample we needed. For the prefabricated Au electrodes, we use ultraviolet lithography and thermal evaporation technology to produce Au electrode patterns on silicon wafer (with 300 nm SiO_2). Similar to the above process, the PVA solution is dripped on the silicon wafer with the prefabricated Au electrodes to obtain a PVA film with the thickness of several hundred micrometers. The ultrathin K-12442 sample and the prefabricated Au electrodes can be transferred by the PVA films from the silicon and SiO_2/Si substrates respectively. Using the three-axis alignment platform, the ultrathin sample and the Au electrodes can be aligned, which are encapsulated between two PVA sheets. Because the ultrathin K-12442 samples are sensitive to the external environment, the packaging of the samples must be completed within half an hour under the atmospheric condition. In the upper left inset of figure 2, we show an optical microscopic picture of the ultrathin sample denoted as S-2. One can see that the sample is transparent and the length of the sample can be as large as 30 μm.

The electrical transport data were collected on the physical property measurement system (Quantum Design, PPMS) by a standard four-probe method using the prefabricated Au electrodes (see figure 1). The external magnetic field H was rotated in the plane perpendicular to the electric current. θ denoted the included angle between H and c axis of the crystal. The applied electric current is 10 μA. The possible influences of this current magnitude on the transport data have been

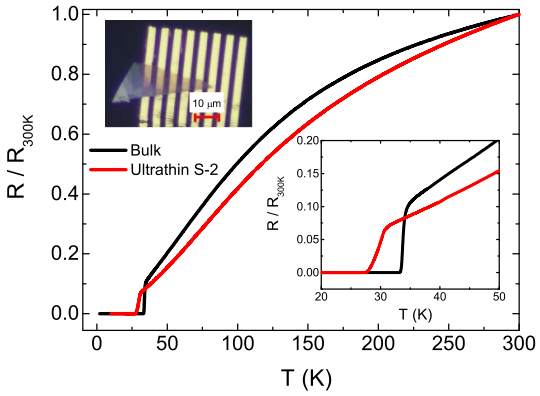

Figure 2. Temperature dependence of normalized resistance of K-12442 ultrathin sample S-2. The data of the bulk sample is also shown for comparison. The upper left inset shows the picture of the sample S-2 under optical microscope. The yellow strips are electrodes. The lower right inset is an enlarged view of the resistance data.

examined. A decreasing of the current by one third only changes the superconducting transition temperature by 0.08 K (see supplementary data (available online at stacks.iop.org/2DM/8/025024/mmedia)). Moreover, the effect on the temperature calibration by the possible poor thermal conductance of PVA was also checked by comparing the temperature dependent resistance data with warming and cooling. As can be seen in the supplementary data, this effect is negligible.

In principal, the strain induced by the different shrinkages between the sample and PVA with cooling may affect the value of T_c, since it is found that T_c is closely related to the structural parameters in the iron-based superconductors [38, 39]. Currently, however, it is difficult to evaluate this effect precisely because the detailed interaction between the sample and PVA is indistinct. Nevertheless, such an effect should not change the main conclusion of the present work that the remarkable dimensionality effect is observed in the ultrathin K-12442 system, especially considering the fact that the field-angular-dependent experiments were carried out at a fixed temperature (see figure 5).

3. Results and discussion

Normalized resistance of ultrathin K-12442 sample S-2, as well as the data of the bulk sample, is shown in figure 2. The thickness of this sample is estimated to be 2.6–5 nm, corresponding to 1–2 unit cells (see supplementary data). Typically the temperature dependent tendency of resistance for the ultrathin sample is very similar to that for the bulk sample, both of which reveal a negative curvature with residual resistance ratio (RRR) above 10. The onset SC transition temperature $T_c^{\rm onset}$ of the ultrathin sample is 30.6 K determined using a criterion of 90% R_n (R_n is the normal state resistance at the SC transition point). This value is slightly lower than that of the bulk sample (33∼34 K). The more significant difference between the ultrathin and bulk samples is the SC transition width ΔT_c. Defined as the width between 10% R_n and 90% R_n, the very small $\Delta T_c = 0.6$ K in the bulk sample is increased to 2.4 K in the ultrathin sample. Such a dimensionality effect on T_c and ΔT_c may reflect the enhancement of quantum fluctuation by the decrease of sample thickness, which is in sharp contrast to that observed in ultrathin cuprates. In the case of Bi2212, the transition width ΔT_c is the same between the bulk and monolayer samples, which is as large as 10 K [19, 21]. Such a comparison evidently indicates that the interlayer coupling in the iron–arsenic superconductors is stronger than that of cuprates, which leads to a more prominent dimensionality effect in the former system.

We next focus on the upper critical field H_{c2} and irreversible field $H_{\rm irr}$ of the ultrathin sample at two different field-orientations. As shown in figures 3(a) and (b), the R–T curves become more broadening with the increase of magnetic field. Such a broadening effect is more significant when the field is parallel to the c axis, which is qualitatively consistent with that observed in bulk samples [36, 40]. We extract the values of H_{c2} and $H_{\rm irr}$ using the criterion of 90% R_n and 10% R_n respectively, which are shown in figure 3(c). It is notable that the in-plane upper critical field H_{c2}^{ab} reveals a very steep increase with cooling near the SC transition. To have a quantitative comparison, the data are plotted together with that of the bulk sample in figures 3(d) and (e). In order to coincide with the $T_c^{\rm onset}$ and $T_c^{\rm zero}$ values of the ultrathin sample, the data of the bulk sample are shifted to lower temperatures. For the upper critical field, as shown in figure 3(d), the behaviors of $H_{c2}^{ab} - T$ is very similar between the ultrathin and bulk samples. Whereas, the H_{c2}^{c} value of the ultrathin sample rises more gently with cooling near $T_c^{\rm onset}$, as compared with the bulk one, which gives rise to a larger anisotropy $\Gamma = H_{c2}^{ab}/H_{c2}^{c}$ near T_c for the ultrathin sample. The detailed values of the slopes $\mathrm{d}\mu_0 H_{c2}^{ab,c}(T)/\mathrm{d}T|_{T_c}$, the anisotropy $\Gamma(T_c)$, along with the information about T_c, are summarized in table 1. One can see that the value of $\mathrm{d}\mu_0 H_{c2}^{ab}(T)/\mathrm{d}T|_{T_c}$ only decreases a bit when sample becomes ultrathin. In contrast, $\mathrm{d}\mu_0 H_{c2}^{c}(T)/\mathrm{d}T|_{T_c}$ is reduced almost by half. The in-plane irreversible field $H_{\rm irr}^{ab}$ is clearly suppressed in the ultrathin sample, resulting in a more broadening flux liquid region when the field is applied within the ab plane. Meanwhile, the out-of-plane $H_{\rm irr}^{c}$ reveals no difference with the bulk sample in the low field region below 2 T and is slightly lower in the higher field region.

Since the thickness of the K-12442 samples has a strong influence on the H–T phase diagram, as observed in figure 3, it is important to further know how it behaves inside the H–T phase diagram. We therefore plot the Arrhenius plots in

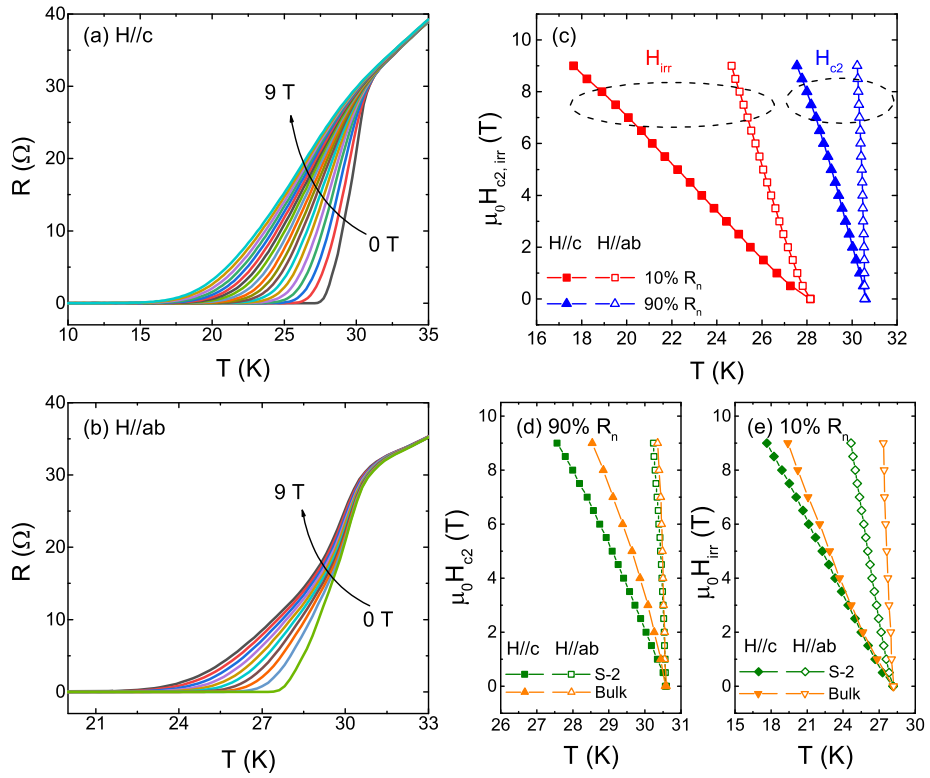

Figure 3. (a), (b) Electrical resistance of the ultrathin sample S-2 as a function of temperature under the magnetic field up to 9 T with H//c and H//ab, respectively. The increasing steps of the fields are 0.5 T and 1 T for the two figures respectively. (c) Upper critical field H_{c2} and irreversible field H_{irr} of the ultrathin sample as a function of temperature for two different orientations. (d), (e) Comparison of H_{c2} and H_{irr} between the ultrathin and bulk samples. In order to have an intuitive comparison, the data of the bulk sample are shifted to lower temperatures by 2.75 and 4.50 K for (d) and (e) respectively.

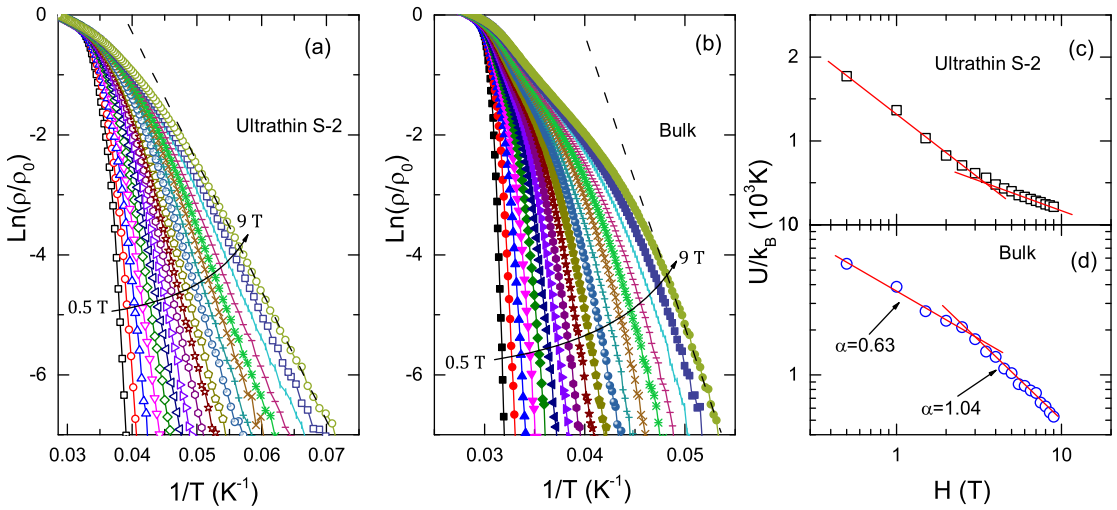

Figure 4. The Arrhenius plots for ultrathin (a) and bulk K-12442 single-crystalline samples (b). The increasing step of the magnetic field is 0.5 T for the two sets of data. The slope of the linear dash lines in (a) and (b) gives the thermal activation energy (U). (c, d) The values of U at various magnetic field (H) for ultrathin and bulk samples respectively. The solid lines are the guide for eyes.

figures 4(a) and (b) for ultrathin and bulk K-12442 single-crystalline samples, respectively. The Arrhenius plot is used to describe the thermal activated flux flow (TAFF) behavior, where the resistivity ρ obeys the relationship $\rho = \rho_0 \exp(-U/k_B T)$ (k_B is the Boltzmann constant and $U(B)$ is the thermally activated energy). Thus $U(B)$ can be obtained from the slope of the linear part in the Arrhenius plot Ln(ρ) vs. T^{-1}. The acquired $U(B)$ at various magnetic fields from 0.5 to 9 T are summarized in figures 4(c) and (d). It is found that $U(B)$ for ultrathin K-12442 (see figure 4(c)) is smaller than the one for bulk sample (see figure 4(d)). Similar results were observed in 2 H-$NbSe_2$, where the activation energy were found to

Table 1. Summary of the detailed parameters about T_c and upper critical fields for both the ultrathin and bulk K-12442.

Sample	T_c^{onset} (K)	T_c^{zero} (K)	ΔT_c (K)	$d\mu_0 H_{c2}^{ab}(T)/dT\|_{T_c}$ (TT/K)	$d\mu_0 H_{c2}^{c}(T)/dT\|_{T_c}$ (TT/K)	$\Gamma(T_c)$
Ultrathin	30.6	28.2	2.4	−47.6	−3.3	14.4
Bulk	33.3	32.7	0.6	−50.9	−6.4	8.0

decrease with decreasing the sample thickness to the 2D limit [41]. Such a behavior is a closely related to the decrease of superfluid stiffness with the reduced layer number. Moreover, for the ultrathin sample, the activation energy U is proportional to lnH with a crossover at around 3.5 T, which suggests a 2D liquid state for the vortices. While for the bulk sample, U shows a $H^{-\alpha}$ dependence, with two parameters α = 0.63 and 1.04 in two field regions, indicating the three-dimensional (3D) feature.

To further explore the dimensionality effect of the ultrathin K-12442 system, we carried out the field-angle resolved experiments by measuring the field and angle (θ) dependence of resistance at a fixed temperature 29.5 K. As shown in figure 5(a), the clear anisotropy of the upper critical field results in the variation of resistance with the orientations of applied field. From this data, we can obtain the field dependence of resistance at different angles, which is shown in figure 5(b). One can see how the resistance is enhanced by the field and even saturates gradually with the increase of field in the low angle region. Due to the very large slope of H_{c2}^{ab} with T ($d\mu_0 H_{c2}^{ab}(T)/dT|_{T_c}$), the increase of resistance is rather limited even under a field of 9 T. Thus a criterion of 75% R_n is adopted to define the upper critical fields. It is notable that the detailed criterion does not change the behavior fundamentally (see supplementary data). Angle dependence of $H_{c2}(\theta)$ normalized by H_{c2}^{c} is shown in figure 5(c), from which one can see the detailed evolution of $H_{c2}(\theta)/H_{c2}^{c}$ versus θ. In order to quantitatively evaluate such an angle dependent variation, we employ two theoretical models, the 3D GL model [42] and 2D Tinkham model [43] (see supplementary data), and plot the curves based on them with the experimental data for comparison. These two models are almost the same in the low-angle region and show slight differences above 80°, which is usually used to distinguish the 2D superconductivity in ultrathin or interfacial systems [6, 44–46]. It is clear that the Tinkham model can better described the experimental data, indicating the 2D characteristic of the superconductivity in the present ultrathin K-12442 system.

Such a 2D feature was not observed in the bulk sample. In the bulk K-12442 system, angle dependence of $H_{c2}(\theta)$ follows a tendency of the 3D GL model (see supplementary data). The evolution from 3D in the bulk sample to 2D behaviors in the ultrathin sample represents clearly the dimensionality effect in this system. To quantitatively understand this behavior, we estimated the values of coherence length ξ near T_c from the upper critical field (see inset of figure 5(c); details for the estimation of ξ see supplementary data). Due to quick increase of H_{c2}^{ab} with cooling near T_c, we can only obtain the values of ξ_c in the temperatures above 30 K. Nevertheless, we still grasp important information that ξ_c is several nanometers at around 30 K and increases quickly in higher temperatures, which is

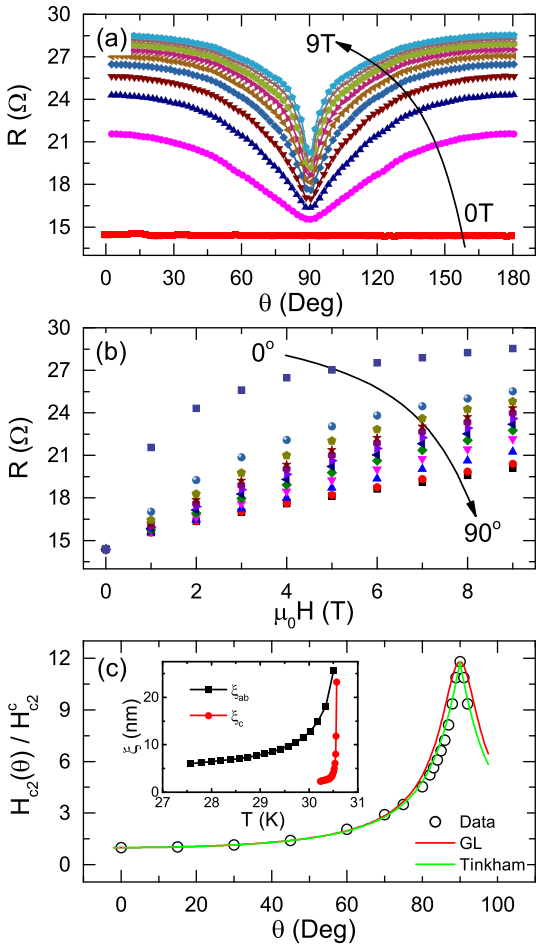

Figure 5. (a) Magnetic field angular dependence of electronic resistance for the ultrathin sample S-2 at 29.5 K under magnetic fields up to 9 T. The increasing step of the field is 1 T. (b) Field dependence of the resistance with the external field rotating from $H//c$ ($\theta = 0°$) to $H//ab$ ($\theta = 90°$) at a fixed temperature $T = 29.5$ K. The increasing steps of the angle are 15°, 5°, and 1° at angle ranges 0°–60°, 70°–80°, and 82°–90°, respectively. (c) Angle dependence of the upper critical field $H_{c2}(\theta)$ normalized by H_{c2}^{c}. The values of $H_{c2}(\theta)$ are determined using a criterion of 75% R_n. The theoretical curves based on the GL and Tinkham models are shown in comparison with the experimental data. The inset shows the temperature dependence of coherence length close to T_c.

in the same order of magnitude with the thickness of the ultrathin sample (2.6–5 nm). This is the internal reason for the observation of the 2D superconductivity. The clear dimensionality effect reveals the importance of interlayer coupling in this iron–arsenic system, especially when compared with cuprate superconductor Bi2212.

4. Conclusions

In summary, we successfully obtained the ultrathin samples of the iron–arsenic superconductor $KCa_2Fe_4As_4F_2$ by using an improved mechanical exfoliation method. The dimensionality effect was observed in terms of the lower T_c, the wider transition width, the higher anisotropy, the broadening flux liquid region, the smaller thermal activated energy with a 2D feature, and more importantly, the 2D evolution in the angle dependence of upper critical field, in the ultrathin samples. Our results reveal the different features between the iron–arsenic and cuprates superconductors, and provide a very unique and suitable platform to investigate the dimensionality effect in unconventional superconductors.

Acknowledgments

This work is supported by the Youth Innovation Promotion Association of the Chinese Academy of Sciences (No. 2015187) and the National Natural Science Foundation of China (Nos. 11204338, 11574338, 51925208, U1632266, U1530402 and 11927807). The fabrications process for device were performed in the Superconducting Electronics Facility (SELF) of Shanghai Institute of Microsystem and Information Technology.

ORCID iDs

Tao Hu https://orcid.org/0000-0003-0338-9632
Hong Xiao https://orcid.org/0000-0001-8859-9967
Wei Peng https://orcid.org/0000-0002-9888-1891
Zengfeng Di https://orcid.org/0000-0002-9357-5107
Gang Mu https://orcid.org/0000-0001-5676-4702

References

[1] Reyren N *et al* 2007 *Science* **317** 1196
[2] Gozar A, Logvenov G, Kourkoutis L F, Bollinger A T, Giannuzzi L A, Muller D A and Bozovic I 2008 *Nature* **455** 782
[3] Saito Y, Nojima T and Iwasa Y 2016 *Nat. Rev. Mater.* **2** 16094
[4] de la Barrera S C *et al* 2018 *Nat. Commun.* **9** 1427
[5] Xi X, Zhao Z, W, Park J-H, Law K T, Berger H, Forro L, Shan J and Mak K F 2016 *Nat. Phys.* **12** 139
[6] Lu J M, Zheliuk O, Leermakers I, Yuan N F Q, Zeitler U, Law K T and Ye J T 2015 *Science* **350** 1353
[7] Tsen A W *et al* 2016 *Nat. Phys.* **12** 208
[8] Phillips P and Dalidovich D 2003 *Science* **302** 243
[9] Ephron D, Yazdani A, Kapitulnik A and Beasley M R 1996 *Phys. Rev. Lett.* **76** 1529
[10] Saito Y, Kasahara Y, Ye J, Iwasa Y and Nojima T 2015 *Science* **350** 409
[11] Berezinskii V L 1971 *Sov. Phys. JETP* **32** 493 (http://www.jetp.ac.ru/cgi-bin/e/index/e/32/3/p493?a=list)
[12] Kosterlitz J M and Thouless D J 1973 *J. Phys.* C **6** 1181
[13] Wang Q-Y *et al* 2012 *Chin. Phys. Lett.* **29** 037402
[14] Pan J *et al* 2017 *J. Am. Chem. Soc.* **139** 4623
[15] Yang Y, Fang S, Fatemi V, Ruhman J, Navarro-Moratalla E, Watanabe K, Taniguchi T, Kaxiras E and Jarillo-Herrero P 2018 *Phys. Rev.* B **98** 035203
[16] Bednorz J G and Müller K A 1986 *Z. Phys.* B **64** 189
[17] Kamihara Y, Watanabe T, Hirano M and Hosono H 2008 *J. Am. Chem. Soc.* **130** 3296
[18] Sandilands L J *et al* 2014 *Phys. Rev.* B **90** 081402
[19] Jiang D *et al* 2014 *Nat. Commun.* **5** 5708
[20] Liao M *et al* 2018 *Nano Lett.* **18** 5660
[21] Yu Y, Ma L, Cai P, Zhong R, Ye C, Shen J, Gu G D, Chen X and Zhang Y 2019 *Nature* **575** 156
[22] Zhao S Y F *et al* 2019 *Phys. Rev. Lett.* **122** 247001
[23] Gray M J *et al* 2019 *Nano Lett.* **19** 4890
[24] Tang F, Wang P P, Wang P, Gan Y, Gu G D, Zhang W, He M and Zhang L 2019 *J. Phys.: Condens. Matter* **31** 265702
[25] Ren Z-A *et al* 2008 *Chin. Phys. Lett.* **25** eid2215
[26] Zhu X, Han F, Mu G, Cheng P, Shen B, Zeng B and Wen H-H 2009 *Phys. Rev.* B **79** 220512(R)
[27] Rotter M, Tegel M and Johrendt D 2008 *Phys. Rev. Lett.* **101** 107006
[28] Wang Z-C, He C-Y, Wu S-Q, Tang Z-T, Liu Y, Ablimit A, Feng C-M and Cao G-H 2016 *J. Am. Chem. Soc.* **138** 7856
[29] Wang Z, He C, Tang Z, Wu S and Cao G 2017 *Sci. China Mater.* **60** 83–89
[30] Wang Z C, He C Y, Wu S Q, Tang Z T, Liu Y, Ablimit A, Tao Q, Feng C M, Xu Z A and Cao G H 2017 *J. Phys.: Condens. Matter* **29** 11LT01
[31] Wang Z-C, He C-Y, Wu S-Q, Tang Z-T, Liu Y and Cao G-H 2017 *Chem. Mater.* **29** 1805
[32] Wu S-Q, Wang Z-C, He C-Y, Tang Z-T, Liu Y and Cao G-H 2017 *Phys. Rev. Mater.* **1** 044804
[33] Wang Z C, Liu Y, Wu S Q, Shao Y T, Ren Z and Cao G H 2019 *Phys. Rev.* B **99** 144501
[34] Zverev V N, Korobenko A V, Sun G L, Sun D L, Lin C T and Boris A V 2011 *Japan. J. Appl. Phys.* **50** 05FD02
[35] Xiao H, Gao B, Ma Y H, Li X J, Mu G and Hu T 2016 *J. Phys.: Condens. Matter* **28** 325701
[36] Wang T, Chu J, Jin H, Feng J, Wang L, Song Y, Zhang C, Xu X, Li W, Li Z, Hu T, Jiang D, Peng W, Liu X and Mu G 2019 *J. Phys. Chem.* C **123** 12925
[37] Cao Y, Wang X, Lin X, Yang W, Lv C, Lu Y, Zhang Y and Zhao W 2020 *IEEE Access* **8** 70488
[38] Lee C-H *et al* 2008 *J. Phys. Soc. Japan* **77** 083704
[39] Mizuguchi Y, Hara Y, Deguchi K, Tsuda S, Yamaguchi T, Takeda K, Kotegawa H, Tou H and Takano Y 2010 *Supercond. Sci. Technol.* **23** 054013
[40] Wang T *et al* 2020 *Sci. China Phys. Mech. Astron.* **63** 227412
[41] Benyamini A *et al* 2019 *Nat. Phys.* **15** 947
[42] Blatter G, Feigel'man M V, Geshkenbein V B, Larkin A I and Vinokur V M 1994 *Rev. Mod. Phys.* **66** 1125
[43] Harper F E and Tinkham M 1968 *Phys. Rev.* **172** 441
[44] Saito Y *et al* 2016 *Nat. Phys.* **12** 144
[45] Zhou W, Xing X, Zhao H, Feng J, Pan Y, Zhou N, Zhang Y, Qian B and Shi Z 2017 *New J. Phys.* **19** 073014
[46] Ma Y, Pan J, Guo C, Zhang X, Wang L, Hu T, Mu G, Huang F and Xie X 2018 *Quantum Mater.* **3** 34